ACS Catalysis

Research Article

pubs.acs.org/acscatalysis

Highly Active Ni/xNa/CeO_2 Catalyst for the Water−Gas Shift Reaction: Effect of Sodium on Methane Suppression

M. L. Ang,[†] U. Oemar,[†] E. T. Saw,[†] L. Mo,[‡] Y. Kathiraser,[†] B. H. Chia,[†] and S. Kawi*[,†]

[†]Department of Chemical and Biomolecular Engineering, National University of Singapore, 4 Engineering Drive 4, Singapore, Singapore 117576

[‡]Institute of Catalysis, Department of Chemistry, Zhejiang University, Tianmushan Road 148, Hangzhou, Zhejiang 310028, PR China

Supporting Information

ABSTRACT: The effect of Na loading on the water−gas shift (WGS) activity of Ni/xNa/CeO_2 (with x = 0, 0.5, 1, 2, 5, and 10 wt %) catalysts has been investigated. Ni/2Na/CeO_2 exhibited the highest performance in terms of WGS activity and methane suppression. Through H_2-TPR and XRD, the solubility limit of Na^+ in CeO_2 was found to be 2 wt %. At low loadings of Na (0.5 to 2 wt %), Na^+ was incorporated into the CeO_2 lattice, generating a lattice strain and activating the lattice O_2, thereby increasing the reducibility of the catalyst. However, beyond the solubility limit of 2 wt %, Na deposited on the CeO_2 surface, retarding the reducibility of the catalyst. XPS spectra reveal greater surface concentration of adsorbed oxygen species with the introduction of Na. This can be attributed to the generation of more oxide vacancies for oxygen adsorption due to Na substitution into the ceria lattice. By in situ DRIFTS, methanation was found to be inhibited by the interaction between Na and Ni, leading to the absence of subcarbonyl species which are responsible for this undesirable side reaction.

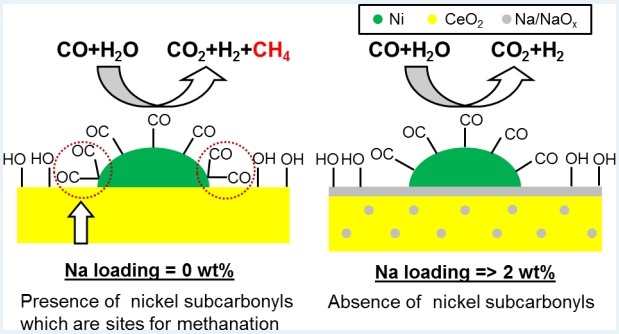

KEYWORDS: *water−gas shift, nickel catalyst, ceria, sodium, DRIFTS*

1. INTRODUCTION

The Water−Gas Shift (WGS) reaction is one of the major processes involved in all carbon-based fuel processes. Its primary purpose is to convert most of the CO to CO_2 while producing and upgrading H_2 from synthetic gas produced from upstream processes such as reforming and gasification:

$$CO + H_2O \leftrightarrow H_2 + CO_2, \quad \Delta H = -41.2\ \text{kJ/mol} \qquad (1)$$

Being a reversible and exothermic reaction, WGS is thermodynamically favored at high temperatures and kinetically favored at low temperatures. This balance between thermodynamics and kinetics results in the reaction being executed in a series of stages industrially, with inter-reactors cooling, so as to achieve a high extent of CO conversion. Industrially, CO concentrations can be decreased from 10 to 50 wt % to 0.3 wt % in a two stage WGS system with interstage cooling.[1] In such a system, Fe_2O_3−Cr_2O_3 based catalysts are employed in the high temperature shift (350−450 °C) and Cu-ZnO based catalysts are used in the low temperature shift (190−250 °C).

Nickel-based catalysts have been widely used for reactions such as steam reforming of methane[2,3] and CO methanation[4−7] owing to its cheap cost and high catalytic performance. However, its application in the WGS reaction has been prohibitive due to its high activity toward an undesirable side reaction−methanation−that would consequently reduce the selectivity toward the WGS reaction and thereby decrease H_2 yield. Therefore, much effort has been devoted into developing nickel-based catalysts that suppress the methanation reaction during the WGS reaction. For instance, Gan and Zhao[8] reported an inverse NiO_{1-x}/Cu catalyst that was able to suppress methanation. They attributed the suppression to the presence of oxidized $Ni^{\delta+}$ species which had weak interaction with CO and low activity toward CO dissociation. Next, Lee et al.[9] investigated the effect of zinc addition into the $NiFe_2O_4$ catalyst, and methane suppression was found to be related to the enhanced redox property of the inverse-spinel species. Recently, a lack of CO methanation activity was also observed by Shinde and Madras for the Pd-modified Ni/CeO_2 catalyst.[10] They attributed it to the creation of oxide vacancies−due to ionic substitution of Pd and Ni into CeO_2−that induces H_2O dissociation, leading to higher activity and selectivity toward the WGS reaction. From the above-mentioned works, it can be seen that oxygen plays an important role in enhancing WGS activity for nickel-based catalysts. Thus, in order to utilize nickel-based catalysts for the WGS reaction, it is necessary to couple it with an oxygen-providing or partially reducible oxide support. This therefore leads us to ceria-based catalysts−a metal oxide that is well-known for its high oxygen storage capacity.

Received: March 7, 2014
Revised: August 11, 2014
Published: August 15, 2014

Ceria has been highly effective and widely applied in catalysis applications due to its high oxygen storage capacity (OSC), enabling it to release oxygen in reducing conditions and to store oxygen in oxidizing conditions.[11] Ceria has been used in formulations of automobile three-way catalysts,[12,13] water gas shift catalysts,[14−18] steam reforming catalysts,[19] catalysts for hydrogenation and oxidation reactions,[20−22] and electrodes of solid oxide fuel cells.[23,24] Upon reduction, removal of an oxygen atom creates an oxygen vacancy site and results in the reduction of Ce^{4+} to Ce^{3+}, with the two remaining electrons localized into the 4f states of two adjacent Ce ions.[25] The reduction of ceria can be expressed in the Kröger-Vink notation as[26]

$$O_O + 2Ce_{Ce} \rightarrow \frac{1}{2}O_2(gas) + V_O^{\cdot\cdot} + 2Ce'_{Ce} \quad (2)$$

where O_O and Ce_{Ce} denote neutral O and Ce in the ceria lattice, $V_O^{\cdot\cdot}$ is a oxygen vacancy site with an effective charge of +2, and Ce'_{Ce} refers to Ce with an effective charge of −1.

Alkali promotion for the WGS reaction has been studied extensively, and significant enhancements have been observed when doping alkali such as Na, Li, and K to a Pt-based catalyst supported on oxide supports such as CeO_2,[27,28] ZrO_2,[29,30] TiO_2,[31,32] Al_2O_3,[31] and activated carbon.[33] Flytzani-Stephanopoulos and co-workers have proposed the promoting effect of alkali, in particular, sodium (or potassium) atoms, to be that of providing oxygen to the active Pt metal site in the form of hydroxyls that are bound to Pt with oxygen links in Pt-Na(K)-$O_x(OH)_y$ clusters.[33−35] Water dissociation occurs on these clusters, forming an −OH group which reacts with CO at low temperatures. Alternative postulation proposed by Davis and co-workers suggests that alkali promotes the WGS reaction by weakening the formate C−H bond, thereby increasing the rate of formate decomposition. This formate decomposition step has been proposed as a rate-determining step for the low-temperature WGS reaction.[27−29] Sodium, in particular, has been widely acclaimed to promote the WGS reaction. Incorporation of Na^+ into t-ZrO_2 supports was found to promote WGS by stabilizing ZrO_2 in the tetragonal phase.[30] The promotional role of Na was also attributed to the strong interaction between Pt and NaO_x and the consequent formation of highly active Pt-NaO_x sites at the interface with the support that enhances WGS.[36] The objective of this work is therefore to study the role of Na in Ni/CeO_2 catalysts in enhancing WGS activity and increasing selectivity toward the WGS reaction, thereby suppressing the unwanted side reaction of methanation. To the best of our knowledge, there is yet to be any studies focusing on Na promotion on Ni-based catalysts for the WGS reaction.

2. EXPERIMENTAL SECTION

2.1. Catalyst Preparation. *2.1.1. Preparation of Na-Doped Ceria Support.* Nanosized ceria support was prepared by the reverse microemulsion method according to a procedure described elsewhere[37] but with slight modifications. The typical procedure for preparing pure CeO_2 support is as follows. Cetyltrimethylammonium bromide (CTAB) (12.132 g) was added to 450 mL of dry toluene and was stirred vigorously for 2 h. Dry toluene was obtained by storing toluene over molecular sieves for 24 h to remove moisture. Subsequently, 5.9814 mL of tetramethylammonium hydroxide (TMAH) was added dropwise to the mixture. After 2 h of stirring, the cerium precursor solution prepared by dissolving 1.8180 g of $Ce(NO_3)_3{\cdot}6H_2O$ (Sigma-Aldrich) dissolved in 13.394 mL of deionized water was added dropwise to the mixture. The microemulsion was then aged for 6 days to allow complete hydrolysis and condensation of Ce^{4+} hydroxyl species to form ceria. To obtain the final product, the resultant mixture was centrifuged for 20 min at 10 000 rpm. The supernatant was decanted, and the residue was washed with ethanol to remove the excess sodium ions and CTAB. This washing and centrifuging process was repeated thrice. Finally, the solid product was dried in a vacuum oven overnight and calcined at a heating rate of 2 °C/min in static air for 2 h.

The calcined pure CeO_2 support was then doped with Na via the wet-impregnation method. Na loading in xNa/CeO_2 supports was varied with x = 0, 0.5, 1, 2, 5, and 10 wt %. The weight percentages of Na refer to the final weight percentages of Na in the respective Ni/xNa/CeO_2 catalysts. The typical procedure for preparing 5Na/CeO_2 support is as follows. $NaNO_3$ (0.076080 g) (Sigma-Aldrich) was dissolved in 10.000 mL of deionized water, and the aqueous solution was then mixed with 0.35000 g of calcined pure CeO_2 support to obtain the required Na loading. The mixture was dried under constant stirring at 80 °C and further dried at 100 °C for another 24 h before it was calcined at 650 °C with a heating rate of 2 °C/min in static air for 2 h.

2.1.2. Nickel Impregnation on Na-Doped Support. Upon yielding the Na-doped CeO_2 supports, an aqueous solution containing the required $Ni(NO_3)_2{\cdot}6H_2O$ (Sigma-Aldrich) was mixed with the requisite amount of Na-doped CeO_2 support to obtain the 10 wt % Ni/xNa/CeO_2 catalysts. The mixtures were then dried under constant stirring at 80 °C and further dried at 100 °C for another 24 h before they were calcined at 650 °C with a heating rate of 2 °C/min in static air for 2 h.

2.2. Catalyst Characterization. *2.2.1. BET Surface Area.* Surface areas of the catalysts were determined via nitrogen adsorption with the Brunauer−Emmett−Teller (BET) method using a Micromeritics ASAP-2020 adsorption apparatus. Prior to analysis, the samples were degassed in vacuum at 350 °C for 4 h, and the N_2 adsorption isotherms were subsequently measured at 77 K.

2.2.2. N_2O Chemisorption. In order to calculate the amount of active sites and metal dispersion, pulse titration was performed on the Quantachrome ChemBET-3000 according to the method reported in recent literature.[38] The H_2-TPR was initially performed using 0.05 g of sample up to 650 °C, followed by cooling down to room temperature. Purified N_2O gas was then introduced to the system by pulse injection until saturation. The H_2-TPR was repeated up to 650 °C. The amount of active sites can be calculated from the amount of adsorbed N_2O, while the dispersion can be calculated by comparing the second TPR to the first TPR results.

2.2.3. X-ray Diffraction (XRD). The X-ray diffraction pattern of each catalyst was measured on a Shimadzu XRD-6000 diffractometer using Cu Kα radiation. The catalyst was placed on a plastic slide and scanned from 2θ of 20° to 80° with a step degree of 0.02°. The beam voltage and current used were 40 kV and 30 mA, respectively. The lattice parameter was determined from Bragg's Law with the intensity of the most prominent peak (200) and (111) for Ni and Ce, respectively. The mean crystallite size of cerium and nickel oxide was estimated through the Scherrer equation by line broadening of (200) and (111) peaks, respectively.

2.2.4. H_2-Temperature-Programmed Reduction (H_2-TPR). Temperature-programmed reduction (TPR) measurement for the fresh catalyst was performed on Quantachrome ChemBET-

dx.doi.org/10.1021/cs500915p | ACS Catal. 2014, 4, 3237−3248

Table 1. Physicochemical Parameters for Ni/xNa/CeO_2 Catalysts

catalyst	BET surface area (m^2/g)	metal dispersion[a] (%)	metal particle[b] size (nm)	crystallite size[c] (nm) Ni [111]	NiO [200]	CeO_2 [111]	lattice parameter[d] (nm) NiO [200]	CeO_2 [111]	H_2 consumption[e] (mmol/g)	reduction degree of NiO[f] (%)
0Na/CeO_2						14.51		5.400	0.40	
0.5Na/CeO_2						14.73		5.402	0.40	
1Na/CeO_2						18.46		5.414	0.46	
2Na/CeO_2						21.67		5.420	0.63	
5Na/CeO_2						20.80		5.420	2.28	
10Na/CeO_2						17.30		5.436	8.82	
Ni/0Na/CeO_2	25.70	20.50	4.93	14.67	20.68	12.32	4.173	5.394	2.89	100
Ni/0.5Na/CeO_2	8.75	15.18	6.66	15.32	26.71	16.87	4.176	5.411	3.16	111
Ni/1Na/CeO_2	4.79	21.03	4.80	13.70	25.74	20.25	4.181	5.418	2.79	93.6
Ni/2Na/CeO_2	7.99	9.72	10.39	15.02	27.12	22.78	4.179	5.418	2.83	88.2
Ni/5Na/CeO_2	2.50	3.36	30.04	24.73	25.51	22.08	4.181	5.420	8.25	240[g]
Ni/10Na/CeO_2	0.42	3.81	26.54	27.42	27.06	19.15	4.180	5.419	12.9	166[g]

[a]Metal dispersion was calculated by N_2O chemisorption. [b]Metal particle size was determined by the expression, d = 101/metal dispersion (%). [c]Crystallite size was determined by XRD with the Scherrer equation. [d]Lattice parameter was determined by the formula, $\alpha = (h^2 + k^2 + l^2)^{1/2}((\lambda)/(2\sin\theta))$. [e]$H_2$ consumption below 900 °C in TPR profiles shown in Figure 2. [f]Reduction degree of NiO (%) = 100 × (H_2 consumed by Ni metal)/($(H_2$ consumed by Ni metal$)_{Ni/0N\alpha/CeO_2}$). [g]Reason for anomalous percentage of reduction degree of NiO can be found in the main text.

3000, equipped with a thermal conductivity detector (TCD). Prior to TPR measurement, 0.05 g of catalyst was outgassed in He for 1 h at 300 °C to remove any impurities and then cooled down to room temperature. 5% H_2/N_2 gas was then introduced at 80 mL/min to the catalyst, while the temperature of the furnace was increased from 50 to 900 °C at a heating rate of 10 °C/min. Quantitative measurement of H_2 consumption over the xNa/CeO_2 supports and Ni/xNa/CeO_2 catalysts were calculated for the derivation of percentage of NiO reduction degree. Assuming the degree of reduction of support in Ni/xNa/CeO_2 catalysts to be completely the same as that of xNa/CeO_2 supports, the amounts of H_2 consumption by the Ni metal on the different Ni/xNa/CeO_2 catalysts were obtained by subtracting H_2 consumption of support from the total H_2 consumption by the Ni/xNa/CeO_2 catalyst.[39] The degree of reduction of NiO on the Ni/0Na/CeO_2 catalyst was assumed to be 100% and used a basis for calculation of reduction degree for other Ni/xNa/CeO_2 catalysts.

2.2.5. X-ray Photoelectron Spectroscopy (XPS). The catalyst surface analysis was performed using X-ray photoelectron spectroscopy (XPS) with a KRATOS AXIS Ultra spectrometer equipped with a monochromatic Al−Kα ($h\nu$ = 1486.71 eV) radiation source operated at 5 mA and 15 kV. The binding energy (BE) was calibrated based on the line position of C 1s (284.50 eV). Prior to XPS analysis, the catalysts were reduced under pure H_2 at 650 °C for 1 h and cooled down to room temperature of about 30 °C before transferring to the sample stub promptly.

2.2.6. Transmission Electron Spectroscopy (TEM). The metal particle size was measured visually using HRTEM system JEOL JEM-2100F. The average metal size was then calculated over 100 particles. Prior to the observation, the catalyst was reduced at 650 °C under H_2 for 1 h. The sample was then ultrasonically dispersed in ethanol and spread over perforated copper grids.

2.2.7. Diffuse Reflectance Fourier Transform Infrared Spectroscopy (DRIFTS). In situ DRIFTS data were collected using a Bruker FTIR spectrometer equipped with a Harrick Praying Mantis DRIFTS cell connected to a gas flow system. The catalyst was reduced at 650 °C for 1 h and cooled down to a room temperature of about 30 °C. Upon H_2 reduction, surface hydroxyl (−OH) groups are formed on the ceria surface by reduction of surface oxygen. Prior to introducing CO and H_2, the reduced catalyst was flushed with He for 10 min to remove residual H_2. Stepwise heating and cooling with an increment of 50 °C up to 600 °C were applied. The temperature was held for 15 min at each step.

2.3. Catalytic Activity Measurements. The catalytic reaction was carried out in a fixed bed quartz reactor with an inner diameter of 4 mm and a length of 400 mm. The catalyst (0.05 g) was used in each test and was sandwiched between two quartz wool plugs in the middle of the reactor. Prior to the catalytic reaction, the catalyst was reduced in 10 mL/min H_2 at 650 °C for 1 h. After H_2-reduction, the reactor temperature ramped down to the desired reaction temperature (300−600 °C) under hydrogen. Water delivered by a HPLC pump, was vaporized at 150 °C in a preheater, and the resultant steam was mixed with reactant gases before entering the reactor. The reactant feed composition was as follows: 5 mol % CO, 25 mol % H_2O, He balance, and the total flow rate was of 50 mL/min with GHSV of about 68000 h^{-1}. The effluent gases were passed through a cold trap which was set at a temperature of 5 °C to condense the unreacted water from the WGS reaction, and the noncondensable product gases were subsequently analyzed by an HP-GC equipped with a Hayesep D column. The data was collected when the reaction had reached steady-state. The stability test was conducted for 100 h using the above-mentioned reactant feed composition. To measure the amount of adsorbed carbon (CH_4 precursor) on the spent catalysts, thermogravimetric analysis (TGA) was conducted using the

dx.doi.org/10.1021/cs500915p | ACS Catal. 2014, 4, 3237−3248

Shimadzu DTG-60 gravimetric analyzer. Around 10 mg of spent catalyst was used in each TGA analysis and heated in air to 800 °C with a heating rate of 10 °C/min.

The total conversion of CO was calculated according to the following equation:

$$X_{CO,total} = \frac{[CO_2]_{out} + [CH_4]_{out}}{[CO]_{out} + [CO_2]_{out} + [CH_4]_{out}} \quad (3)$$

Correspondingly, CO conversion to CO_2 was calculated according to the following equation:

$$X_{CO} = \frac{[CO_2]_{out}}{[CO]_{out} + [CO_2]_{out} + [CH_4]_{out}} \quad (4)$$

In the absence of methanation (i.e., production of CH_4), the above equation reduces to the following equation:

$$X_{CO,WGS} = \frac{[CO_2]_{out}}{[CO]_{out} + [CO_2]_{out}} \quad (5)$$

The CH_4 and H_2 yields are calculated according to the following equation:

$$\%CH_4\ (H_2)\ \text{Yield} = \frac{[CH_4]_{out}([H_2]_{out})}{[CO_2]_{out} + [H_2]_{out} + [CH_4]_{out}} \quad (6)$$

For turnover frequency (TOF) calculations and derivation of reaction rates, the catalytic activity testing was performed with diluted catalysts (diluted with powder quartz SiO_2) with a total flow rate of 100 mL/min in order to maintain a total CO conversion of below 10%. The TOF was calculated according to the following equation:

$$\text{TOF} = \frac{\text{mol of CO converted}}{\text{mol of Ni metal} \times \text{time (s)}} \quad (7)$$

The rate of reaction was calculated using the following equation:

$$\text{Rate} = \frac{\text{mol of } H_2 \text{ produced}}{\text{mass of catalyst (g)} \times \text{time (s)}} \quad (8)$$

3. RESULTS AND DISCUSSION

3.1. BET – Surface Area Analysis. Table 1 shows the BET surface area of Ni/xNa/CeO_2 catalysts. It was observed that the surface areas of the catalysts decreased greatly with increasing loading of Na. This is primarily due to the penetration of Na into the pores of ceria support during impregnation, resulting in the blockage of pores and a subsequent decrease in the surface area. Besides, different loadings of Na can also affect the texture of ceria to variable extents.

3.2. N_2O Chemisorption–Metal Dispersion. The metal dispersion in reduced Ni/xNa/CeO_2 catalysts was measured using N_2O chemisorption. As shown in Table 1, metal dispersion decreased upon increasing Na loading. This is largely due to the reduction in surface area with higher Na loadings. However, as evident from the catalytic results, lower metal dispersion in higher Na loading Ni/CeO_2 catalysts did not decrease the activity greatly.

3.3. X-ray Diffraction (XRD) – Structural Analysis. The catalysts were analyzed using XRD to identify the crystalline phases, and the XRD patterns for the fresh, calcined catalysts are shown in Figure 1(a). The cubic fluorite structure of CeO_2 (JCPDS No. 00-043-1002) and the face-centered cubic

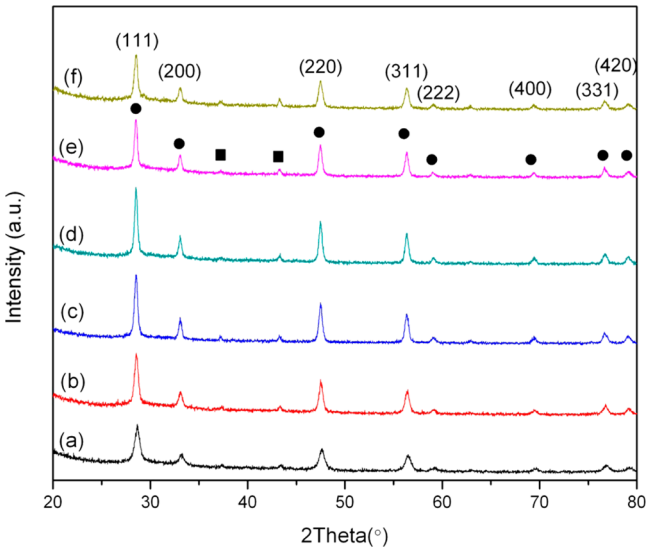

Figure 1. XRD patterns of freshly calcined (a) Ni/0Na/CeO_2, (b) Ni/0.5Na/CeO_2, (c) Ni/1Na/CeO_2, (d) Ni/2Na/CeO_2, (e) Ni/5Na/CeO_2, and (f) Ni/10Na/CeO_2 catalysts. Circles denote CeO_2 phase and squares denote NiO phase.

structure of NiO (JCPDS No. 04-0835) are apparent in all samples. Table 1 displays the lattice parameters and crystallite sizes of NiO and CeO_2 derived using Bragg's law and Scherrer's equation, respectively. The average crystallite sizes of NiO were determined by line broadening of (200) line of NiO at about 2θ = 43.3°. Ni crystallite sizes were estimated to be 20.7, 26.7, 25.7, 27.1, 25.5, and 27.1 nm for Ni/0Na/CeO_2, Ni/0.5Na/CeO_2, Ni/1Na/CeO_2, Ni/2Na/CeO_2, Ni/5Na/CeO_2, and Ni/10Na/CeO_2 catalysts, respectively. Similarly, average crystallite sizes for CeO_2 were determined by line broadening of (111) at about 2θ = 28.6° and were approximated to be 12.3, 16.9, 20.3, 22.8, 22.1, and 19.2 nm for Ni/0Na/CeO_2, Ni/0.5Na/CeO_2, Ni/1Na/CeO_2, Ni/2Na/CeO_2, Ni/5Na/CeO_2, and Ni/10Na/CeO_2 catalysts, respectively. Upon introduction of Na, the NiO crystallite size increases abruptly from 20.7 to 26.7 nm and remains approximately constant when Na loading was increased from 0.5 wt % to 10 wt %. However, in the case of CeO_2 crystallite size, a monotonic increase in CeO_2 crystallite size was observed with increasing Na loading from 0 wt % to 2 wt %. Beyond 2 wt %, CeO_2 crystallite size gradually decreases as Na loading was increased from 5 wt % to 10 wt %. This volcanic trend can be explained by the change in grain boundary mobility brought about by different Na loadings. At low Na loading of 0.5 wt % to 2 wt %, Na^+ cations diffuse and incorporate into the CeO_2 lattice, thereby generating oxygen vacancies which enhance the grain boundary mobility.[40,41] However, beyond the solubility limit of 2 wt %, increasing Na loading results in the suppression of grain boundary mobility due to solute drag effect.[40,42] A steep Na concentration gradient between the bulk and intergrain interfaces is formed when excess Na is deposited on the CeO_2 surface boundaries. This Na solute gradient then generates a strong drag to the grain boundary mobility, suppressing grain growth and reducing the CeO_2 size.[42] A similar trend was also observed by Lee et al.,[41] in which the grain size of gadolinia-doped ceria was found to increase with increasing Ga_2O_3 content up to 5 mol % and then decreased with further introduction of Ga_2O_3. In order to show the presence of reduced metal on the reduced Ni/xNa/CeO_2 catalysts, a narrow scan was performed, and the result is shown

dx.doi.org/10.1021/cs500915p | ACS Catal. 2014, 4, 3237–3248

in Figure S1 (see the Supporting Information). The average crystallite sizes of Ni were determined by line broadening of (111) line of Ni at about $2\theta = 44.4°$. Ni crystallite sizes were estimated to be 14.7, 15.3, 13.7, 15.0, 24.7, and 27.4 nm for Ni/0Na/CeO_2, Ni/0.5Na/CeO_2, Ni/1Na/CeO_2, Ni/2Na/CeO_2, Ni/5Na/CeO_2, and Ni/10Na/CeO_2 catalysts, respectively. Likewise, a similar upward trend in the metallic Ni crystallite size is observed as Na loading was increased.

From Table 1, it is evident that the lattice parameter of Ce increased linearly from 5.394 Å (in Ni/0Na/CeO_2) to 5.418 Å (in Ni/1Na/CeO_2) and remains approximately constant. This observation is consistent with Vegard's law. This increase can be attributed to the substitution of bigger Na^+ ions (1.18 Å) for Ce^{4+} ions (0.97 Å)[43,44] which generates a lattice expansion and forms oxygen vacancies because of charge compensation. At Na loadings close to the solubility limit of 2 wt %, lattice expansion reaches a maximum of about 5.418 Å. Therefore, increasing Na loading beyond 2 wt % does not increase the lattice parameter further.

3.4. H_2-Temperature-Programmed Reduction (H_2-TPR) – Reducibility Analysis. H_2-TPR profiles for Ni/xNa/CeO_2 catalysts are reported in Figure 2. In general, two

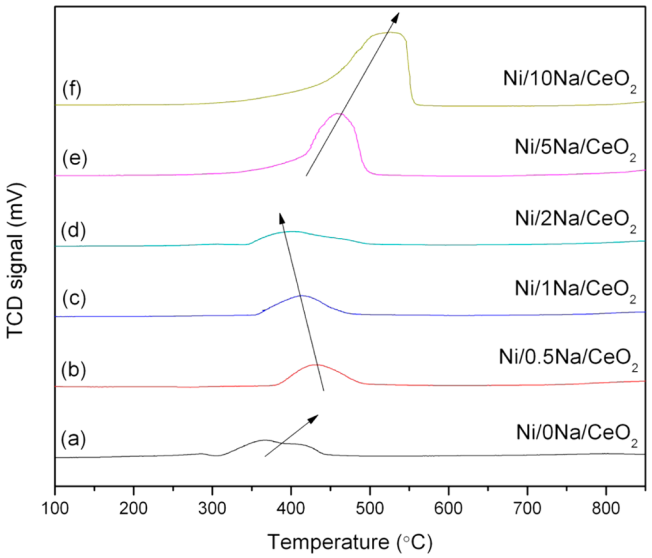

Figure 2. H_2-TPR profiles of (a) Ni/0Na/CeO_2, (b) Ni/0.5Na/CeO_2, (c) Ni/1Na/CeO_2, (d) Ni/2Na/CeO_2, (e) Ni/5Na/CeO_2, and (f) Ni/10Na/CeO_2 catalysts.

main reduction peaks can be discerned. The first reduction peak centered at about 400 °C can be attributed to the reduction of Ni^{2+} to Ni^0 and probably to the reduction of surface capping oxygen of ceria,[45] while the broad reduction peak started at around 850 °C can be attributed to the reduction of bulk oxygen in CeO_2. As compared to other Na-doped catalysts, Ni/0Na/CeO_2 has an additional subtle low temperature peak at 320 °C which can be ascribed to free NiO particles.[46] An interesting phenomenon was observed as Na loading was varied from 0 to 10 wt %. Initially, as Na loading was increased from 0 wt % to 0.5 wt %, the main reduction peak shifted to higher temperature from 367 °C (in Ni/0Na/CeO_2) to 430 °C (in Ni/0.5Na/CeO_2). However, further increment in Na loading from 0.5 wt % to 2 wt % shifted the main reduction peak from 430 °C (in Ni/0.5Na/CeO_2) to 413 °C (in Ni/1Na/CeO_2) and subsequently to 403 °C (in Ni/2Na/CeO_2). Interestingly, upon further increment in Na loading to 5 and 10 wt %, this reduction peak shifted in the opposite direction to even higher temperatures of 458 and 525 °C, respectively. At the onset, the addition of 0.5 wt % Na increased the reduction temperature due to the stronger interaction between Ni and the Na-doped CeO_2 support. However, further introduction of Na from 0.5 wt % to 2 wt % increases the reducibility of the catalyst due to the incorporation of Na^+ into the CeO_2 lattice, resulting in lattice distortion and creation of oxygen vacancies. It has been reported that Na^+ (ionic radius of 1.18 Å), due to its similar ionic radius to that of Ce^{4+} (0.97 Å), has a high possibility of incorporating into the ceria lattice.[46] Factoring in the high calcination temperature of 650 °C, there is a great likelihood that a solid solution, $Na_xCe_{1-x}O_{2-y}$, was formed between Ce and Na. Thus, it is expected that at low Na loadings of 0.5 wt % to 2 wt %, Na was incorporated into the CeO_2 lattice, leading to a lattice expansion as observed from the XRD results stated above. This lattice distortion and generation of oxygen vacancies increase the oxygen mobility and in turn enhance the reducibility of the catalyst.[47] Song and Ozkan have reported enhanced oxygen mobility in the Co/CeO_2 catalyst by incorporation of Ca, which in turn increased the H_2 yield and TOF over the Ca-doped Co/CeO_2 catalyst in the ethanol steam reforming reaction.[48] Shinde and Madras[49] have made a similar observation, whereby ionic substitution of bimetallic Cu–Ni and Cu–Fe was found to activate lattice oxygen in CeO_2, increasing the reducibility and oxygen storage capacity of bimetallic substituted CeO_2. With the inclusion of more sodium, the ceria lattice could no longer accommodate more sodium due to its solubility limit and the excess sodium deposited on the surface of ceria support. Despite the increased reducibility conferred by the doping of Na into CeO_2 lattice, the excess Na that formed an overlayer resulted in an overall decrease in reducibility of the catalyst at higher Na loadings of 5 and 10 wt % due to stronger interactions between Ni and Na possibly through the formation of Ni–O_x–Na complexes.[34,35] The phenomenon of shifting to higher reduction temperatures had also been observed in the case of the alkali-doped Pt/CeO_2 catalyst,[27] the K-doped Co/SiO_2 catalyst,[50] and alkali-doped Pd/Fe_2O_3 catalysts.[51] The deposition of excess Na can also be inferred from the H_2 uptake values tabulated in Table 1. From Table 1, it is evident that H_2 uptake remains relatively constant for 0 wt % to 2 wt % Na loading. However, as Na loading increased from 2 wt % to 10 wt %, H_2 uptake increased from 2.83 mmol H_2/g (in Ni/2Na/CeO_2) to 8.25 mmol H_2/g (in Ni/5Na/CeO_2) and then further increased to 12.9 mmol H_2/g (in Ni/10Na/CeO_2). Since the Ni nominal loading is consistent at 10 wt % for all catalysts, the H_2 uptake required for reduction of Ni^{2+} to Ni^0 should be similar among all catalysts. Thus, this sharp increase in H_2 uptake observed in 5 and 10 wt % Na-doped catalysts can be attributed to the reduction of excess Na_2O deposited on the surface of CeO_2 supports. As shown in Table 1, the reduction degree of NiO is approximately 100% for Ni/xNa/CeO_2 catalysts except for Ni/5Na/CeO_2 and Ni/10Na/CeO_2 catalysts. A possible reason for obtaining reduction degree of >150% for Ni/5Na/CeO_2 and Ni/10Na/CeO_2 catalysts is an underestimation of the H_2 consumption of 5Na/CeO_2 and 10Na/CeO_2 supports due to the partial reduction of the supports in the presence of excess Na. Therefore, the H_2 uptake values also further affirm that the solubility limit of Na^+ within the CeO_2 lattice is 2 wt %. Beyond

dx.doi.org/10.1021/cs500915p | ACS Catal. 2014, 4, 3237–3248

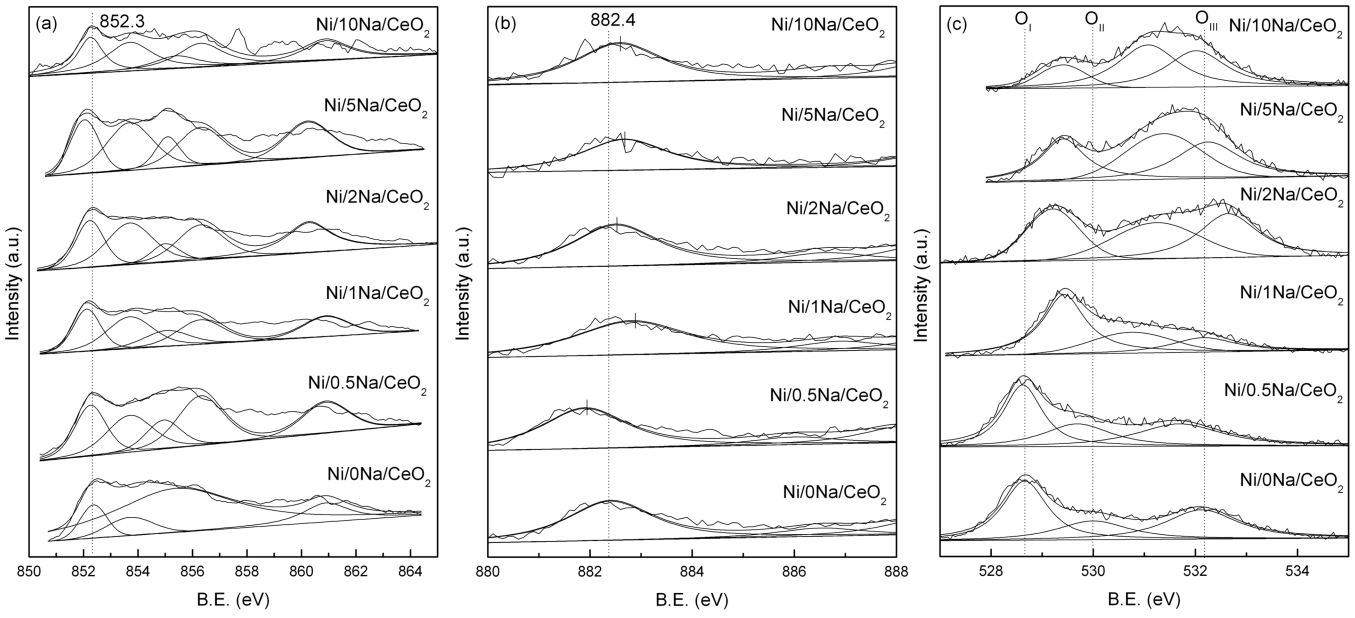

Figure 3. XPS spectra of Ni/xNa/CeO_2 catalysts for (a) Ni 2p, (b) Ce 3d, and (c) O 1s.

Table 2. Surface Composition Derived from XPS

	oxygen concn (%)			cerium concn (%)		nickel ratio	surface composition (at %)			
catalyst	lattice oxygen	adsorbed oxygen	adsorbed water	$[Ce^{3+}]$	$[Ce^{4+}]$	$[Ni^0]/[Ni^{2+}]$	O	Ni	Na	Ce
$Ni/0Na/CeO_2$	43.1	22.1	34.8	13.7	86.3	0.649	76.84	2.77	0	20.39
$Ni/0.5Na/CeO_2$	40.9	26.2	32.8	12.6	87.4	0.677	72.45	2.13	3.89	21.53
$Ni/1Na/CeO_2$	56.0	25.1	18.9	10.4	89.6	0.888	68.47	3.48	6.83	21.21
$Ni/2Na/CeO_2$	30.1	32.6	37.3	10.1	89.7	0.950	70.47	1.86	9.68	18.00
$Ni/5Na/CeO_2$	29.5	36.7	33.8	9.30	90.7	0.419	72.98	2.19	13.28	11.55
$Ni/10Na/CeO_2$	14.3	46.8	38.9	9.87	90.1	0.712	67.65	1.90	20.63	9.82

the solubility limit of 2 wt %, excess Na deposits on the surface of CeO_2 support as Na_2O.

3.5. X-ray Photoelectron Spectroscopy (XPS). An XPS study was conducted on the reduced Ni/xNa/CeO_2 catalysts in order to understand the oxidation states of the various surface species present during reaction. Figure 3(a) displays the Ni ($2p_{3/2}$) spectra of the reduced Ni/xNa/CeO_2 catalysts. The binding energies (BEs) of Ni metal and its satellite peak are 852.6 and 856.3 eV, respectively. Similarly, the BEs of Ni^{2+} in NiO and its two satellite peaks are 855.4 eV, 853.7, and 860.9 eV, respectively.[52] As evident from Figure 3(a), as Na loading is increased from 0 wt % to 5 wt %, there is a clear shift in BE of Ni^0 from 852.3 to 852.1 eV. The downward shift of the Ni 2p BEs observed in Na-doped Ni/xNa/CeO_2 catalysts is indicative of interaction between Na and Ni and that the presence of Na^+ ions increases the electron density on the Ni metal.[53] The Ni 2p spectra was deconvoluted corresponding to the Ni^0 and Ni^{2+} states, and the relative concentrations of the two states were calculated from the deconvoluted peaks. The relative concentration, Ni^0/Ni^{2+}, was found to be 0.649, 0.677, 0.888, 0.950, 0.419, and 0.712 for $Ni/0Na/CeO_2$, $Ni/0.5Na/CeO_2$, $Ni/1Na/CeO_2$, $Ni/2Na/CeO_2$, $Ni/5Na/CeO_2$, and $Ni/10Na/CeO_2$ catalysts, respectively. XPS results of Ni/xNa/CeO_2 catalysts reveal that addition of Na facilitates the reduction of Ni in the Na-doped catalysts as shown by the higher relative concentration of Ni^0/Ni^{2+} for Na-doped catalysts. As shown later in DRIFTS study, nickel metal serves as the active metal sites for catalyzing the WGS reaction, thus greater ease in reduction of Ni^{2+} to Ni^0 is essential in achieving excellent WGS activity.

Figure 3(b) shows the core level spectrum for Ce 3d which is relatively complex due the presence of both Ce^{3+} and Ce^{4+} states. A total of 10 peaks were fitted: 3 doublets for CeO_2 and 2 doublets for Ce_2O_3. The 6 characteristic peaks for CeO_2 are labeled as v (882.4 eV), v″ (888.7 eV), v‴ (898.2 eV), u (900.9 eV), u″ (907.3 eV), and u‴ (916.5 eV). On the other hand, the 4 characteristic peaks for Ce_2O_3 are labeled as v_0 (880.4 eV), v′ (886.5 eV), u_0 (898.7 eV), and u′ (902.9 eV).[10,54] As compared to the $Ni/0Na/CeO_2$ catalyst, there is a significant shift in binding energy toward higher region. This indicates the possibility of Na^+ into CeO_2 lattice, leading to charge imbalance and lattice distortion of CeO_2. This distortion in turn generates oxygen vacancies, enabling oxygen adsorption on these vacancies.[17,54] This finding correlates well with the H_2-TPR results, which showed the shift toward lower reduction temperatures with the incorporation of up to 2 wt % Na.

Figure 3(c) shows the core level spectrum of O 1s. Three peaks are observed in the O 1s region. The first peak (O_I) at around 529 eV can be attributed to lattice oxygen (O^{2-}) in the ceria lattice, the second peak (O_{II}) at around 530 eV corresponds to adsorbed oxygen species, while the third peak (O_{III}) at around 532 eV corresponds to adsorbed water.[55] Similar to the Ce 3d spectra, with the introduction of Na, the binding energies generally shift toward higher binding energies. Table 2 presents the surface composition of the reduced Ni/xNa/CeO_2 catalysts. Evidently, as Na loading increases,

dx.doi.org/10.1021/cs500915p | ACS Catal. 2014, 4, 3237−3248

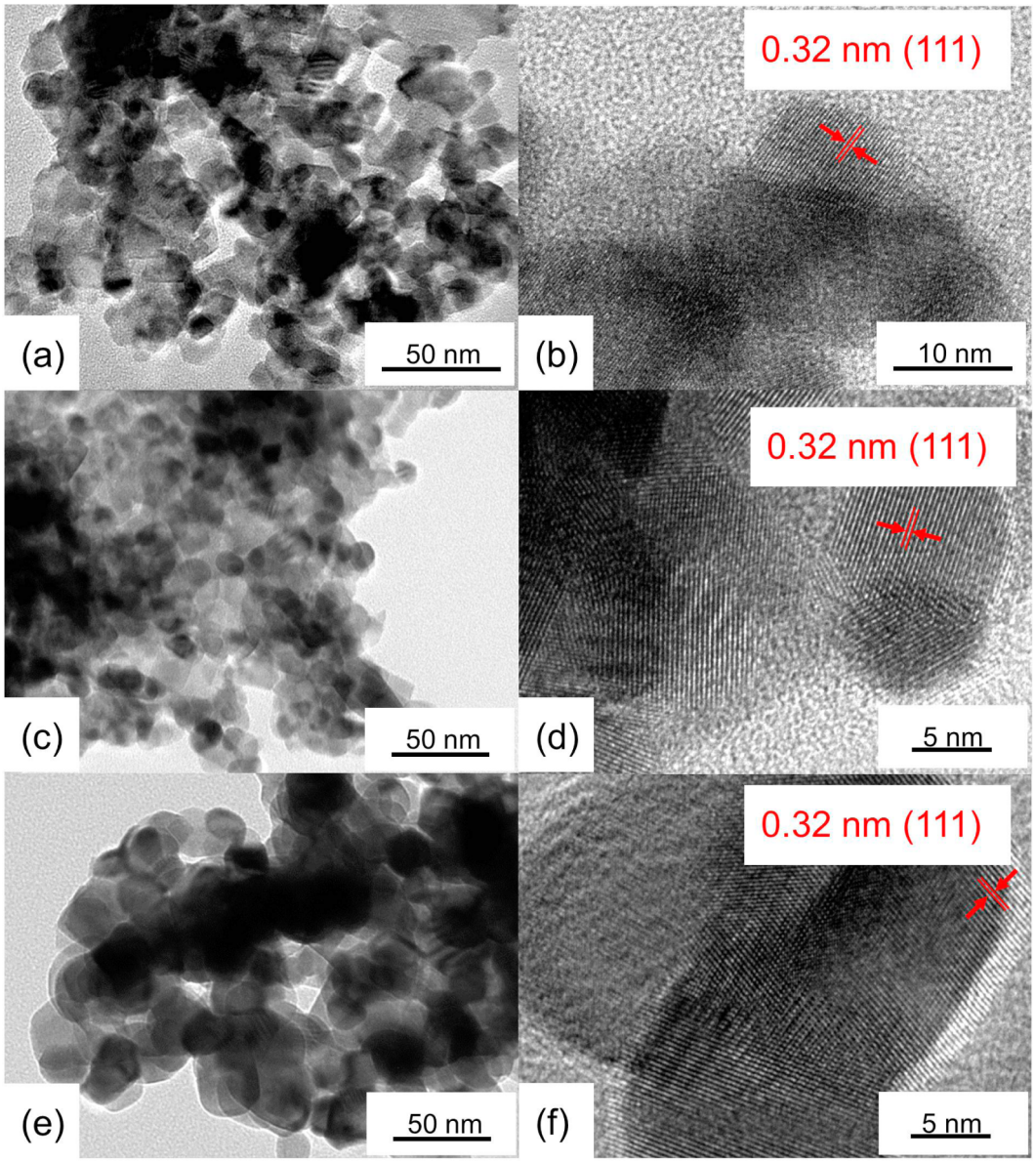

Figure 4. HRTEM images of reduced (a,b) Ni/0Na/CeO_2, (c,d) Ni/2Na/CeO_2, and (e,f) Ni/5Na/CeO_2 catalysts.

concentration of lattice oxygen decreases, while concentration of adsorbed oxygen increases. This result is in agreement with the inference made from Ce 3d spectra as well as the H_2-TPR results that the inclusion of Na^+ into CeO_2 lattice generates oxygen vacancies which lead to a higher amount of oxygen adsorption. The surface compositions of the reduced catalysts are also shown in Table 2. The surface Na concentration increases as Na loading increases, even at low Na loadings of 0 to 2 wt %. This trend may seemingly suggest that Na is deposited on the surface. However, bearing in mind that the sampling depth is generally approximately 3−10 nm depending on the mean free path of the photoelectrons in the material,[56] the surface Na content detected could possibly include the a contained in the ceria lattice. Moreover, it can be seen that the surface concentration of Ce remains approximately constant at about 18−20 at % with Na loading of 0 to 2 wt %. At higher Na loadings of 5 and 10 wt %, surface concentration of Ce drastically decreases to about 10 at%. This result further affirms the postulation that beyond 2 wt % Na loading, excess Na forms an overlayer on ceria particles, thereby reducing the surface Ce concentration.

3.6. Metal Particle Size of Reduced Catalysts. Figure 4 shows the HRTEM images of the reduced catalysts. From Figures 4(a), 4(c), and 4(d), the particle size of CeO_2 are measured to be approximately 15.3 nm, 23.1 nm, and 23.6 nm for Ni/0Na/CeO_2, Ni/2Na/CeO_2, and Ni/5Na/CeO_2 catalysts, respectively. The order of the ceria size is in agreement with quantitative analysis of crystal size obtained using XRD. In addition, as shown in Figures 4(b), 4(d), and 4(f), the lattice fringes are well-defined, thus confirming the crystalline nature of the sample. The width of lattice fringe of 0.32 nm corresponds to (111) CeO_2. The metal particle size of Ni was unable to be clearly distinguished as they could possibly be buried underneath the ceria particles that have agglomerated partially after calcination at 650 °C. From the elemental mapping of the Ni/2Na/CeO_2 catalyst as shown in Figure 5, Ni particle size can be estimated to be about 13.53 nm, which is similar to the particle size obtained via N_2O chemisorption (10.39 nm). In addition, Figure 5(b) which shows the

dx.doi.org/10.1021/cs500915p | ACS Catal. 2014, 4, 3237−3248

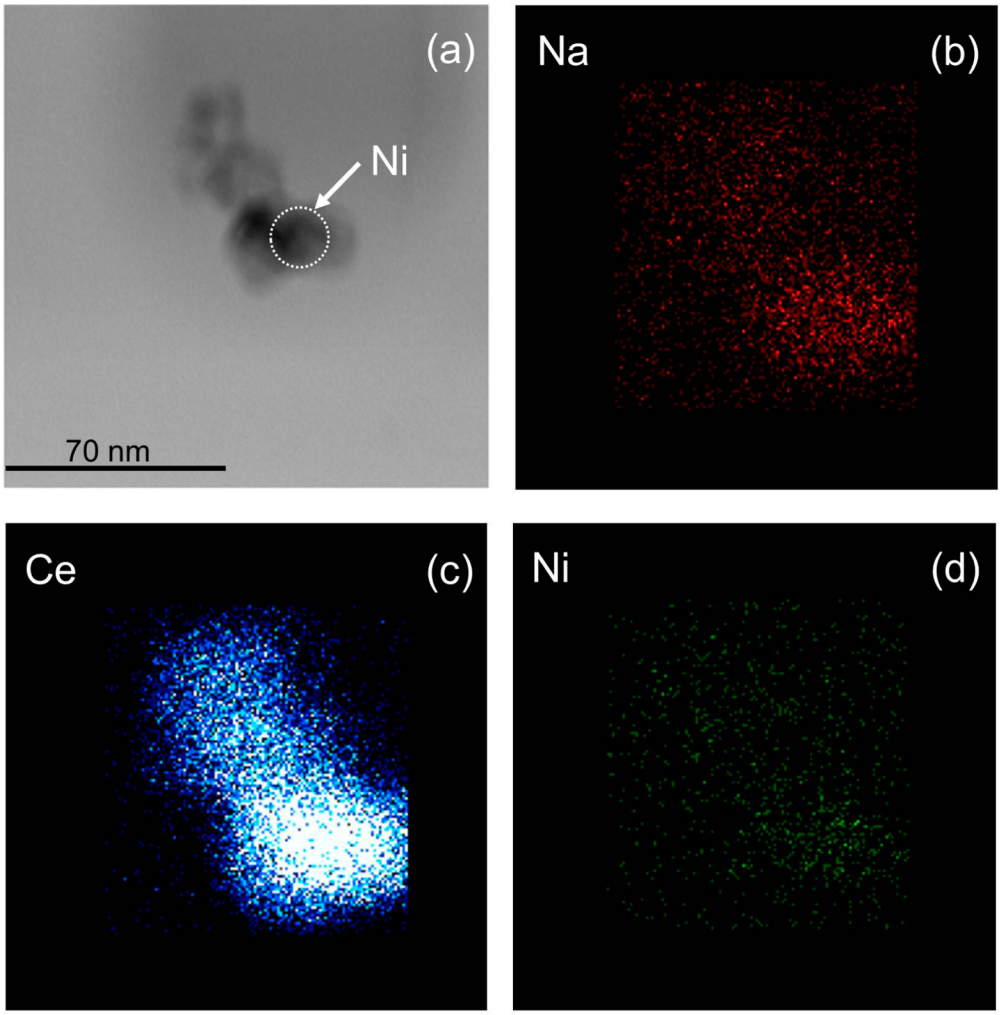

Figure 5. (a) HRTEM image of Ni/2Na/CeO_2 catalyst and (b-d) corresponding EDS mapping images of (a) for Na, Ce, and Ni elements, respectively.

elemental mapping of Na on the Ni/2Na/CeO_2 catalyst reveals that Na is well dispersed on the CeO_2 supports and do not agglomerate, further affirming the formation of Na−Ce−O solid solution.

3.7. Catalytic Activity and Selectivity. Catalytic testing was conducted from 300 to 600 °C, and Figure 6(a) displays the percentage of CO conversion to CO_2 against the reaction temperature for the Ni/*x*Na/CeO_2 catalysts. In general, Na-doped catalysts achieved better catalytic performance as compared to the Ni/0Na/CeO_2 catalyst over the entire temperature range, with the Ni/2Na/CeO_2 catalyst exhibiting the most superior performance. At 400 °C, the Ni/2Na/CeO_2 catalyst achieved a CO conversion of 97.5%, which is very close to that of the theoretical equilbrium level of CO conversion of 98.1%. As Na doping increases beyond 2 wt % to 5 and 10 wt %, CO conversion decreases slightly to 97.1% and 94.4%, respectively. It has been shown that for Pt/CeO_2 catalysts, increasing the alkali amount to levels that are too high will reduce the BET surface area of the catalyst, block the Pt surface sites, and in turn reduce WGS activity. In contrast, at low levels of alkali, alkali promotes the WGS activity by weakening the formate C−H bond significantly.[27] Indeed, from BET analysis, the same trend of drastic reduction in surface area at high levels of Na doping was also observed. This could be the main attribute for the slight deterioration in catalytic activity observed in Ni/5Na/CeO_2 and Ni/10Na/CeO_2 catalysts. Besides displaying excellent WGS activity in terms of CO conversion to CO_2, the activity enhancement by the Ni/2Na/CeO_2 catalyst was accompanied by an increase in selectivity toward the WGS reaction. Figure 6(b) shows the percentages of CH_4 and H_2 yields at 400 °C for all catalysts. As evident from Figure 6(b), CH_4 yield is the highest at 1.93% for the Na-free Ni/0Na/CeO_2 catalyst and abruptly decreases to a low value of 0.52% with the addition of 0.5 wt % Na before gradually decreasing to a gradual plateau as Na was increased from 0.5 to 10 wt %. Consequently, the Ni/0Na/CeO_2 catalyst has the lowest H_2 yield of 43.5% while Na-doped catalysts generally achieved high H_2 yield of at least 46.0%. Therefore, incorporation of 2 wt % Na into the Ni/CeO_2 catalyst was able to enhance the WGS activity, increase the selectivity toward the WGS reaction, and effectively suppress the side reaction, methanation.

Besides, the stability test conducted for 100 h as shown in Figure 7 reveals that Ni/2Na/CeO_2 is catalytically stable and remains selective toward the WGS reaction throughout the 100 h runtime. Postreaction characterization of the spent catalyst shows that the Ni metal crystallite size increased slightly from 15.0 to 20.4 nm (shown in Figure S2) and TGA analysis (shown in Figure S3(b) of the Supporting Information) reveals no deposition of carbon (CH_4 precursor) on the spent catalyst.

dx.doi.org/10.1021/cs500915p | *ACS Catal.* 2014, 4, 3237−3248

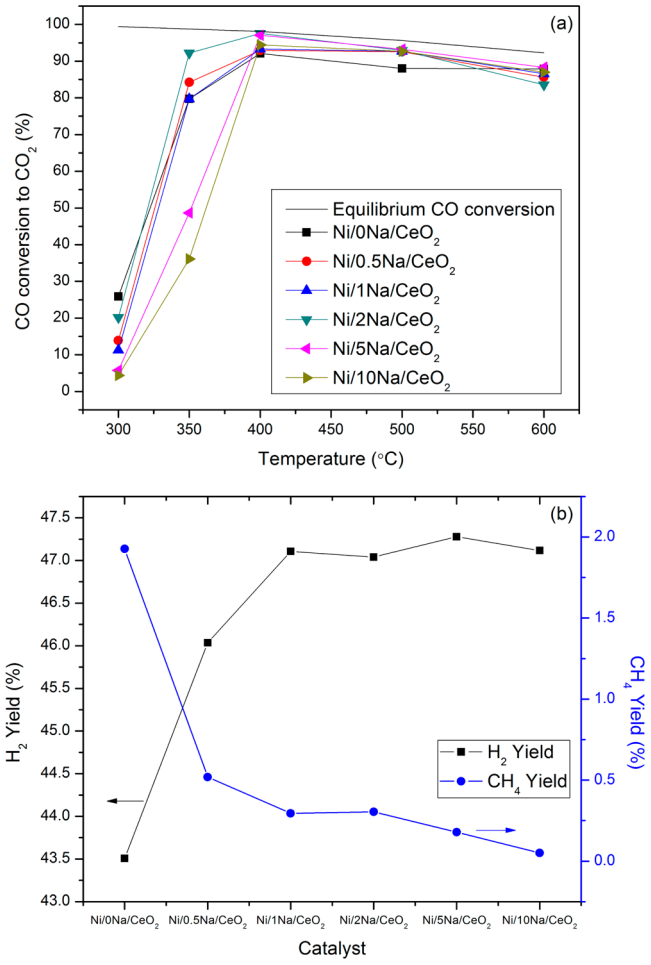

Figure 6. (a) Percentages of CO conversion to CO_2 and (b) H_2 and CH_4 percentage yields for Ni/xNa/CeO_2 catalysts.

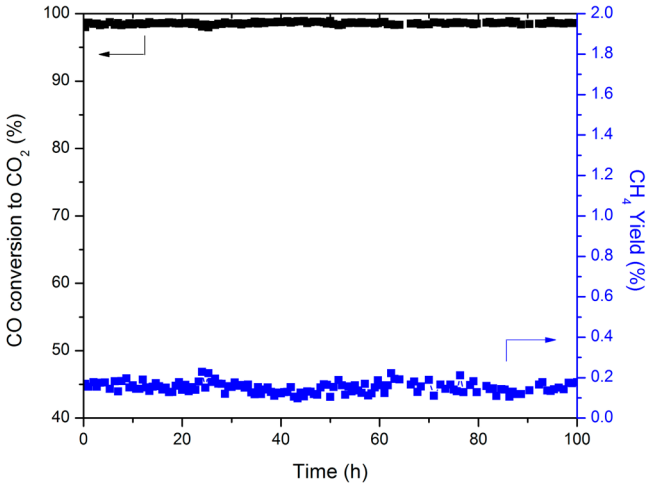

Figure 7. Percentages of CO conversion to CO_2 (left axis) and CH_4 yield (right axis) of the Ni/2Na/CeO_2 catalyst for 100 h reaction.

In addition, XPS analysis of the spent Ni/2Na/CeO_2 catalyst indicates no noticeable changes in the surface concentration of Na from the catalyst. The surface atomic concentrations of Na on the Ni/2Na/CeO_2 catalyst are 9.7 at % and 7.7 at% before and after the reaction, respectively. The stability test for 100 h was also conducted for the the Ni/0Na/CeO_2 catalyst. As compared to the Ni/2Na/CeO_2 catalyst, it has a lower CO conversion and a higher CH_4 yield. Contrary to that of the Ni/2Na/CeO_2 catalyst, TGA analysis of the spent Ni/0Na/CeO_2 catalyst (shown in Figure S3(a) of the Supporting Information) shows deposition of adsorbed carbon (CH_4 precursor) after 100 h runtime, affirming the presence of adsorbed carbon as an intermediate for CH_4 formation.

In addition, the activity of the Ni/2Na/CeO_2 catalyst was also compared with other catalysts found in the literature. The calculated TOF values and rate of hydrogen formation as well as the various operating conditions used in testing of different catalyst systems have been tabulated in Table 3. As evident from Table 3, the current Ni/2Na/CeO_2 catalyst has a lower TOF value than the Pt-based catalyst as reported by Zhu et al.[36] that was tested at 300 °C. However, it showed more superior performance (in terms of TOF and hydrogen formation rate) as compared to a conventional catalyst[57] and other Ni-based catalysts[58,59] at higher temperature regions of >350 °C. A TOF value of 0.46 s^{-1} and a hydrogen formation rate of 75.4 μmol/gcat·s was achieved with the Ni/2Na/CeO_2 catalyst. Hence, the Ni/2Na/CeO_2 catalyst is a promising and highly active catalyst which can be utilized for the WGS reactions conducted at higher temperatures of approximately 400 °C

3.8. In Situ Diffuse Reflectance Infrared Fourier Transform Spectroscopy (DRIFTS). *3.8.1. Interaction with CO-H_2 from 30 to 400 °C.* To investigate the role of Na on the suppression of methane during the WGS reaction, DRIFTS study was conducted by subjecting the reduced catalyst with continuous flow of CO and H_2 to simulate CO hydrogenation conditions. Figure 8(a) shows the FTIR spectra of the Ni/0Na/CeO_2 catalyst reduced at 650 °C and subjected to continuous flow of CO and H_2. At the carbonylic region, two bands at 2014 and 2035 cm^{-1} can be observed at 30 °C. The band at 2014 cm^{-1}, assigned to CO linearly adsorbed on metallic Ni (Ni-CO), increases in intensity as the temperature was raised from 30 to 200 °C. The increment in intensity of linear carbonyl suggests that CO is strongly chemisorbed on metallic nickel, and there is a buildup of surface linear monocarbonyl which eventually decomposed completely at 250 °C. Below 250 °C, the rate of linear CO decomposition is much slower than its adsorption, thus explaining the increase in intensity of the linear monocarbonyl band. In addition, a weak band observed at 2035 cm^{-1} can be assigned to CO on Ni modified by hydrogen atoms introduced during the reduction process. The assignment of this band is similar to that of Tabakova et al. where they have assigned 2040 cm^{-1} to be CO on $Au^{\delta-}$ modified by hydrogen atoms.[60] At 150 °C, a broad shoulder band at 2086 cm^{-1}, assigned to subcarbonyl nickel species $Ni(CO)_n$ (n = 2 or 3), appears and is red-shifted down to 2064 cm^{-1} as temperature was increased to 250 °C.[61] This subcarbonyl band eventually disappears at 300 °C. Concurrently, a significant increase of the bands at 1370, 1565, 2843, and 2928 cm^{-1} due to the formate species adsorbed on reduced Ce^{3+} is also observed. The formation of formates is also accompanied by a gradual increase in intensity of negative band centered at 3662 cm^{-1} related to doubly bridging OH (Type II) species on Ce^{3+}.[27,62] Subsequently, from 300 to 400 °C, a small band at 3016 cm^{-1}, assigned to gaseous CH_4, can also be observed.[61,63] The disappearance of the subcarbonyl band at 300 °C followed by the subsequent appearance of the gaseous CH_4 band suggests that subcarbonyl species are precursors for methane formation.

dx.doi.org/10.1021/cs500915p | ACS Catal. 2014, 4, 3237−3248

Table 3. Comparison of Water−Gas Shift Rates of the Ni/2Na/CeO_2 Catalyst with Other Literature Findings and the Conventional Catalyst

catalyst	conditions	T (°C)	TOF (s^{-1})	rate (μmol H_2/gcat·s)	ref
Ni/2Na/CeO_2	7% CO, 22% H_2O, 10% CO_2, 20% H_2, balance He	400	0.46	75.4	this work
5Ni5Cu/CeO_2	7% CO, 22% H_2O, 10% CO_2, 20% H_2, balance He	350	0.013	18.5	54
3.9Pt/t-ZrO_2	6.8% CO, 21.9% H_2O, 8.5% CO_2, 37% H_2, balance Ar	250	0.4	40.0	30
1Pt-3Na-SiO_2	11% CO, 26% H_2O, 7% CO_2, 26% H_2, balance He	270	0.1−0.8	26.0	34
Pt/TiO_2	2.83% CO, 5.66% H_2O, 37.7% H_2, balance He	300	0.36	6.98	36
Pt-4Na/TiO_2	2.83% CO, 5.66% H_2O, 37.7% H_2, balance He	300	3.82	58.6	36
0.5Pt/0.06Na-TiO_2	3% CO, 10% H_2O, balance He	250	1.58	38.4	32
$Ce_{0.75}Cu_{0.1}Ni_{0.15}O_{2-\delta}$	1.3% CO, 35% H_2O, balance N_2	240		2.20	49
Ni_{20}/$CeLaO_x$	10% CO, 20% H_2O, balance He	400		35.6	58
CuO/Zn/Al_2O_3	7% CO, 22% H_2O, 8.5% CO_2, 37% H_2, balance Ar	200		7.60	57
1Re-10Ni/CeO_2	5% CO, 10% H_2O, balance He	300		30.0	59

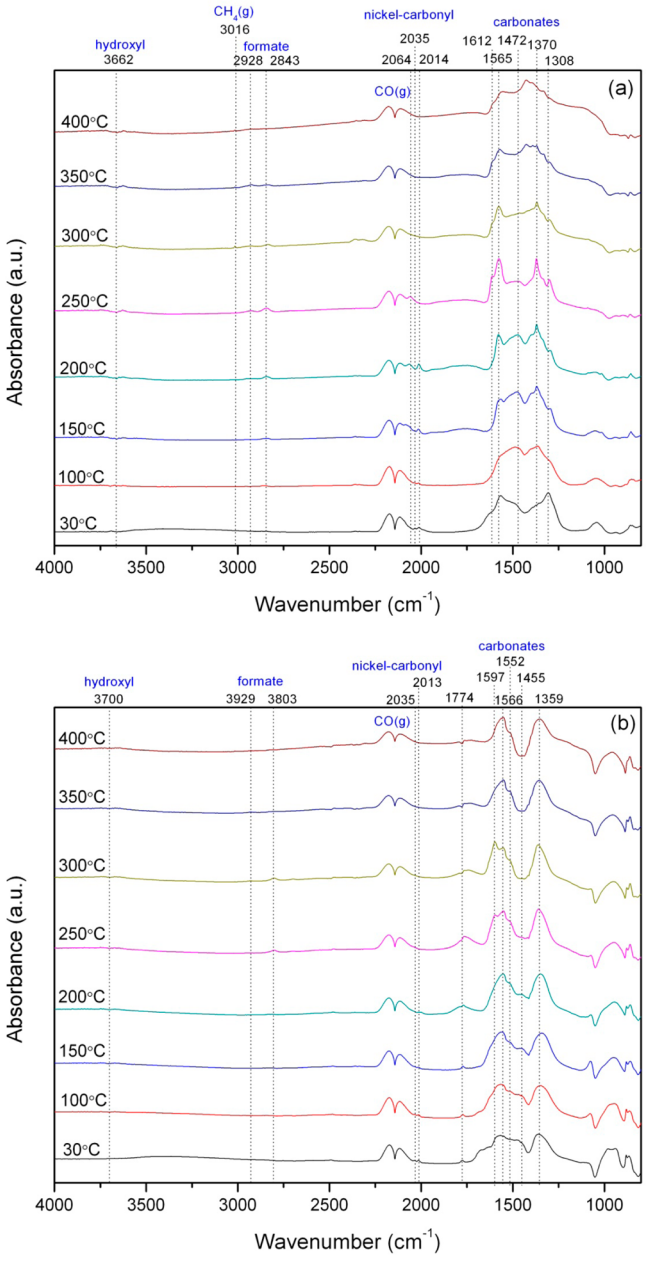

Figure 8. FTIR spectra of (a) Ni/0Na/CeO_2 and (b) Ni/2Na/CeO_2 catalysts under continuous flow of CO and H_2 at temperature increments of 50 °C.

The FTIR spectra of the Ni/2Na/CeO_2 catalyst that is subjected to the same treatment is displayed in Figure 8(b). Similar to the Ni/0Na/CeO_2 catalyst, two carbonyl bands at 2013 and 2035 cm^{-1} assigned to linear monocarbonyl and carbonyl adsorbed on H-modified nickel can be observed at 30 °C, respectively. Unlike the Ni/0Na/CeO_2 catalyst, there was no increase in intensity observed for the band at 2013 cm^{-1}. Instead, the band red-shifted down from 2013 to 2003 cm^{-1} as the temperature was raised from 30 to 200 °C, indicating a weaker C−O bond and a consequently stronger adsorption of linear monocarbonyl on nickel. Another stark contrast between the two catalysts is the absence of subcarbonyl nickel species at 2064 cm^{-1}. In the literature, it was observed in metals such as nickel and ruthenium that subcarbonyl metal species form preferentially on low coordinated nickel species at kink, corner, or step positions.[61,64,65] The absence of this species in the Ni/2Na/CeO_2 catalyst suggests that Ni does not exist as in a low coordinated state due to its interaction with Na.

It has also been reported that alkali additives can migrate from the surface to the nickel surface. Additionally, the DFT calculation study conducted by Bengaard et al.[66] has demonstrated that a stepped nickel surface is more active than close-packed terraces for reforming reaction and its reverse methanation process. This study has also concluded that alkali additives such as sodium preferentially adsorb to highly uncoordinated nickel atoms at step defect sites, thus blocking the active step sites that are responsible for catalyzing the methanation process. Likewise, Nakano et al.[67] investigated the carbon deposition from CO on a Ni (977) surface and found that CO dissociates at step edges. Building on these simulation works, we hypothesize that Na^+ may exist at the step/kink sites of Ni particles, blocking CO dissociation. Hence, DRIFTS studies were further conducted to study the interaction of Ni and Na, and it was found that subcarbonyl species do not form in the presence of Na.

Formate formation was also observed in the case of the Ni/2Na/CeO_2 catalyst, as shown by the gradual increase in the intensity of weak bands at 1359, 1566, 2804, and 2929 cm^{-1} from 250 to 300 °C. In the main formate ν(C−H) stretching band region, Binet et al. have ascribed the band at ca. 2950 cm^{-1} to a coupling of the ν_s(OCO) mode with δ(CH) and the lower wavenumber of ca. 2845 cm^{-1} to ν(C−H) to bridge-bonded formate.[68] As compared to the Ni/0Na/CeO_2 catalyst, there is a clear decrease in the band position of ν(C−H) of the Ni/2Na/CeO_2 catalyst, where there was insignificant change in the band assigned to ν_s(OCO) mode with δ(CH). This observation is consistent with Evin et al. where an obvious

dx.doi.org/10.1021/cs500915p | ACS Catal. 2014, 4, 3237−3248

decrease in the band position for ν(C−H) was observed for alkali-doped Pt/ceria catalysts.[27] The shift to a lower wavenumber from 2843 cm^{-1} in the Ni/0Na/CeO_2 catalyst to 2803 cm^{-1} in the Ni/2Na/CeO_2 catalyst suggests that doping sodium had an impact on the strength of the C−H bond. As summarized by Evin et al.,[27] the effect of doping alkali can be due to three main reasons. The first possibility is alkali metal can exert an electronic effect on the molecule, inducing the weakening of the formate C−H bond, resulting in the shift to a lower band position. The second postulation is the charge transfer from alkali to ceria, indirectly affecting the strength of the formate C−H bond. The third reason proposed is alkali induces geometric or electronic changes such that the bonding of formate can transform from a bidentate mode to another mode such as monodentate. The delayed onset of formate formation on the Ni/2Na/CeO_2 catalyst suggests that the reactivity of CO with OH groups on Ce^{3+} is lower in the Ni/2Na/CeO_2 catalyst than that of the Ni/0Na/CeO_2 catalyst. This can be attributed to the presence of more strongly held CO in Ni/2Na/CeO_2 than in Ni/0Na/CeO_2, inhibiting the formation of formates at lower temperatures. In addition, unlike the Ni/0Na/CeO_2 catalyst, no gaseous CH_4 was observed at 300 °C and beyond, indicating that the Ni/2Na/CeO_2 catalyst is not selective toward CO hydrogenation to CH_4. The presence of formates in both Ni/0Na/CeO_2 and Ni/2Na/CeO_2 catalysts suggests that formate species serve as intermediates of the WGS reaction or as spectators. From the above observations, it is unlikely that these formate species are the precursors for methane formation since they are also present in the Ni/2Na/CeO_2 catalyst that has been shown to suppress methane formation during the WGS reaction.

Deposition of carbon by CO dissociation and the subsequent formation of adsorbed hydrocarbon species have been reported to occur more readily on sites for weakly held CO than on sites for strongly held CO.[65,69,70] Since subcarbonyl nickel species are more weakly held than linearly adsorbed CO, the subcarbonyl sites are more prone to carbon deposition than their linear counterparts. Hence, in the presence of nickel subcarbonyl species, the Ni/0Na/CeO_2 catalyst has a higher tendency to form surface carbonaceous species which are precursors for methane formation as compared to the Ni/2Na/CeO_2 catalyst which does not possess the subcarbonyl species.

3.9. The Role of Na Doping in Ni/*x*Na/CeO_2 Catalysts.

As proposed by Flytzani-Stephanopoulos and co-workers, alkali promotion (such as Na and K) serves to provide oxygen-containing (OH) species to the Pt atoms supported on silica that is otherwise not present, unlike on reducible ceria.[33−35] In the current system of Ni/2Na/CeO_2, similar phenomenon of oxygen-containing species was also observed. In addition to that, new insights with regards to the synergistic effect between Na and CeO_2 were also found to exist in the Ni/*x*Na/CeO_2 catalysts. Through H_2-TPR and XPS, it was shown that the inclusion of 2 wt % Na was able to increase the reducibility of the catalyst by generating oxygen vacancies which allows for greater adsorption of oxygen species. Hence, the use of reducible ceria as a support was able to generate more sites for oxygen adsorption as compared to nonreducible supports, such as SiO_2. Shinde and Madras have also attributed enhanced WGS rates to higher H_2O dissociation induced by the creation of oxide vacancies due to ionic substitution of Pd and Ni ions into the ceria lattice.[10] However, in the current system, the use of Na as a dopant was not only able to generate oxide vacancies, Na itself was also capable of providing oxygen species. Therefore, the synergism between Na and CeO_2 led to enhanced WGS rates observed with the Ni/2Na/CeO_2 catalyst. Moreover, through DRIFTS studies, it was found that the interaction between Ni and Na resulted in less low-coordinated Ni particles which consequently hindered the formation of subcarbonyl species that are the precursors for CH_4 formation. The suppression of methane also played an important role in the enhancement of WGS rates.

4. CONCLUSION

The role of sodium in suppressing methanation during WGS activity can be summarized into two main attributes. First, within the solubility limit of 2 wt %, Na^+ displaces Ce^{4+} in the CeO_2 lattice, generating oxygen vacancies and thereby increasing oxygen mobility. The enhanced oxygen mobility as evident from H_2-TPR is reflected in the highest catalytic activity achieved by the Ni/2Na/CeO_2 catalyst. Second, methane production, which is generally agreed to undergo CO disproportionation and subsequent hydrogenation to CH_4, is largely inhibited in the presence of Na through the interaction of Na and Ni, possibly at step sites. Further DFT calculations and EXAFS studies have to be conducted to prove the hypothesis that Na^+ is located at the step sites of Ni particles. Through this work, it was found that the interaction of Na and Ni leads to the absence of low coordinated Ni species, thereby preventing the formation of subcarbonyl nickel species which are the precursors for the CO methanation reaction.

■ ASSOCIATED CONTENT

Supporting Information

XRD patterns of reduced Ni/*x*Na/CeO_2 catalysts (Figure S1), XRD pattern of spent Ni/2Na/CeO_2 catalyst after 100 h reaction (Figure S2), and TGA profiles of spent Ni/0Na/CeO_2 and Ni/2Na/CeO_2 catalysts after 100 h reaction (Figure S3). This material is available free of charge via the Internet at http://pubs.acs.org.

■ AUTHOR INFORMATION

Corresponding Author

*Phone: +65-6516 6312. Fax: +65-6779 1936. E-mail: chekawis@nus.edu.sg.

Notes

The authors declare no competing financial interest.

■ ACKNOWLEDGMENTS

The authors gratefully thank the National University of Singapore, National Environmental Agency (NEA-ETRP Grant No. 1002114 and RP No. 279-000-333-490) for generously supporting this work.

■ REFERENCES

(1) Ratnasamy, C.; Wagner, J. P. *Catal. Rev.* **2009**, *51*, 325−440.
(2) Xu, J.; Froment, G. F. *AIChE J.* **1989**, *35*, 88−96.
(3) García-Vargas, J. M.; Valverde, J. L.; Lucas-Consuegra, A. D.; Gomez-Monedero, B.; Sanchez, P.; Dorado, F. *Appl. Catal., A* **2012**, *431−432*, 49−56.
(4) Czekaj, I.; Loviat, F.; Raimondi, F.; Wambach, J.; Biollaz, S.; Wokaun, A. *Appl. Catal., A* **2007**, *329*, 68−78.
(5) Hu, D.; Gao, J.; Ping, Y.; Jia, L.; Gunawan, P.; Zhong, Z.; Xu, G.; Gu, F.; Su, F. *Ind. Eng. Chem. Res.* **2012**, *51*, 4875−4886.
(6) Kim, S. H.; Nam, S.-W.; Lim, T.-H.; Lee, H.-I. *Appl. Catal., B* **2008**, *81*, 97−104.

(7) Mok, Y. S.; Kang, H.-C; Lee, H.-J.; Koh, D. J.; Shin, D. N. *Plasma Chem. Plasma Process.* **2010**, *30*, 437−447.
(8) Gan, L.-Y.; Zhao, Y.-J. *J. Phys. Chem. C* **2012**, *116*, 16089−16092.
(9) Lee, M. S.; Lee, J. Y.; Lee, D.-W.; Moon, D. J.; Lee, K.-Y. *Int. J. Hydrogen Energy* **2012**, *37*, 11218−11226.
(10) Shinde, V. M.; Madras, G. *Appl. Catal., B* **2013**, *132*−*133*, 28−38.
(11) Skorodumova, N. V.; Simak, S. I.; Lundqvist, B. I.; Abrikosov, I. A.; Johansson, B. *Phys. Rev. Lett.* **2002**, *89*, 166601.
(12) Kašpar, J.; Fornasiero, P.; Graziani, M. *Catal. Today* **1999**, *50*, 285−298.
(13) Jen, H.-W.; Graham, G. W.; Chun, W.; McCabe, R. W.; Cuif, J.-P.; Deutsch, S. E.; Touret, O. *Catal. Today* **1999**, *50*, 309−328.
(14) Jacobs, G.; Patterson, P. M.; Williams, L.; Chenu, E.; Sparks, D.; Thomas, G.; Davis, B. H. *Appl. Catal., A* **2004**, *262*, 177−187.
(15) Jacobs, G.; Davis, B. H. *Appl. Catal., A* **2007**, *333*, 192−201.
(16) Andreeva, D.; Ivanov, I.; Ilieva, L.; Abrashev, M. V. *Appl. Catal., A* **2006**, *302*, 127−132.
(17) Li, Y.; Fu, Q.; Flytzani-Stephanopoulos, M. *Appl. Catal., B* **2000**, *27*, 179−191.
(18) Fu, Q.; Saltsburg, H.; Flytzani-Stephanopoulos, M. *Science* **2003**, *301*, 935−8.
(19) Srinivas, D.; Satyanarayana, C. V. V.; Potdar, H. S.; Ratnasamy, P. *Appl. Catal., A* **2003**, *246*, 323−334.
(20) Martínez-Arias, A.; Fernandez-Garcia, M.; Galvez, O.; Coronado, J. M.; Anderson, J. A.; Conesa, J. C.; Soria, J.; Munuera, G. *J. Catal.* **2000**, *195*, 207−216.
(21) Zhao, S.; Gorte, R. J. *Appl. Catal., A* **2004**, *277*, 129−136.
(22) Guerrero-Ruiz, A.; Sepúlveda-Escribano, A.; Rodríguez-Ramos, I. *Appl. Catal., A* **1994**, *120*, 71−83.
(23) Park, S.; Vohs, J. M.; Gorte, R. J. *Nature* **2000**, *404*, 265−267.
(24) Eguchi, K.; Setoguchi, T.; Inoue, T.; Arai, H. *Solid State Ionics* **1992**, *52*, 165−172.
(25) Fabris, S.; Gironcoli, S. D.; Baroni, S.; Vicario, G.; Balducci, G. *Phys. Rev. B* **2005**, *71*, 041102.
(26) Kehoe, A. B.; Scanlon, D. O.; Watson, G. W. *Chem. Mater.* **2011**, *23*, 4464−4468.
(27) Evin, H. N.; Jacobs, G.; Ruiz-Martinez, J.; Thomas, G. A.; Davis, B. H. *Catal. Lett.* **2008**, *120*, 166−178.
(28) Linganiso, L. Z.; Jacobs, G.; Azzam, K. G.; Graham, U. M.; Davis, B. H.; Cronauer, D. C.; Kropf, A. J.; Marshall, C. L. *Appl. Catal., A* **2011**, *394*, 105−116.
(29) Pigos, J. M.; Brooks, C. J.; Jacobs, G.; Davis, B. H. *Appl. Catal., A* **2007**, *328*, 14−26.
(30) Xie, H.; Lu, J.; Shekhar, M.; Elam, J. W.; Delgass, W. N.; Ribeiro, F. H.; Weitz, E.; Poeppelmeier, K. R. *ACS Catal.* **2013**, *3*, 61−73.
(31) Pazmiño, J. H.; Shekhar, M.; Williams, W. D.; Akatay, M. C.; Miller, J. T.; Delgass, W. N.; Ribeiro, F. H. *J. Catal.* **2012**, *286*, 279−286.
(32) Panagiotopoulou, P.; Kondarides, D. I. *J. Catal.* **2009**, *267*, 57−66.
(33) Zugic, B.; Bell, D. C.; Flytzani-Stephanopoulos, M. *Appl. Catal., B* **2014**, *144*, 243−251.
(34) Zhai, Y.; Pierre, D.; Si, R.; Deng, W.; Ferrin, P.; Nilekar, A. U.; Peng, G.; Herron, J. A.; Bell, D. C.; Saltsburg, H.; Mavrikakis, M.; Flytzani-Stephanopoulos, M. *Science* **2010**, *329*, 1633−1636.
(35) Wang, Y.; Zhai, Y.; Pierre, D.; Flytzani-Stephanopoulos, M. *Appl. Catal., B* **2012**, *127*, 342−350.
(36) Zhu, X.; Shen, M.; Lobban, L. L.; Mallinson, R. G. *J. Catal.* **2011**, *278*, 123−132.
(37) Yeung, C. M. Y.; Yu, K. M. K.; Fu, Q. J.; Thompsett, D.; Petch, M. I.; Tsang, S. C. *J. Am. Chem. Soc. Comm.* **2005**, *127*, 18010−18011.
(38) Tada, S.; Yokoyama, M.; Kikuchi, R.; Haneda, T.; Kameyama, H. *J. Phys. Chem. C* **2013**, *117*, 14652−14658.
(39) Dong, W.-S.; Roh, H.-S.; Jun, K.-W.; Park, S.-E.; Oh, Y.-S. *Appl. Catal., A* **2002**, *226*, 63−72.
(40) Chen, P.-L.; Chen, I.-W. *J. Am. Ceram. Soc.* **1996**, *79*, 1793−1800.
(41) Lee, J.-S.; Choi, K. H.; Ryu, B.-K.; Shin, B.-C.; Kim, I.-S. *Mater. Res. Bull.* **2004**, *39*, 2025−2033.
(42) Inaba, H.; Nakajima, T.; Tagawa, H. *Solid State Ionics* **1998**, *106*, 263−268.
(43) Shannon, R. D.; Prewitt, C. T. *Acta Crystallogr.* **1969**, *25*, 925−946.
(44) Shannon, R. D.; Prewitt, C. T. *Acta Crystallogr.* **1970**, *26*, 1046−1048.
(45) Wang, Y.; Zhu, A.; Zhang, Y.; Au, C. T.; Yang, X.; Shi, C. *Appl. Catal., B* **2008**, *81*, 141−149.
(46) Pashalidis, I.; Theocharis, C. R. *Stud. Surf. Sci. Catal.* **2000**, *128*, 643−652.
(47) Shan, W.; Luo, M.; Ying, P.; Shen, W.; Li, C. *Appl. Catal., A* **2003**, *246*, 1−9.
(48) Song, H.; Ozkan, U. S. *J. Phys. Chem. A* **2010**, *114*, 3796−3801.
(49) Shinde, V. M.; Madras, G. *Appl. Catal., B* **2012**, *123*−*124*, 367−378.
(50) Jacobs, G.; Das, T. K.; Zhang, Y.; Li, J.; Racoillet, G.; Davis, B. H. *Appl. Catal., A* **2002**, *233*, 263−281.
(51) Watanabe, R.; Sakamoto, Y.; Yamamuro, K.; Tamura, S.; Kikuchi, E.; Sekine, Y. *Appl. Catal., A* **2013**, *457*, 1−11.
(52) Biesinger, M. C.; Paynem, B. P.; Lau, L. W. M.; Gerson, A.; Smart, R. S. C. *Surf. Interface Anal.* **2008**, *41*, 324−332.
(53) Liotta, L. F.; Martin, G. A.; Deganello, G. *J. Catal.* **1996**, *164*, 322−333.
(54) Saw, E. T.; Oemar, U.; Tan, X. R.; Du, Y.; Borgna, A.; Hidajat, K.; Kawi, S. *J. Catal.* **2014**, *314*, 32−46.
(55) Oemar, U.; Ang, M. L.; Hee, W. F.; Hidajat, K.; Kawi, S. *Appl. Catal., B* **2014**, *148*−*149*, 231−232.
(56) Vij, D. R. *Handbook of Applied Solid State Spectroscopy*; Springer, New York, 2006.
(57) Koryabkina, N. A.; Phatak, A. A.; Ruettinger, W. F.; Farrauto, R. J.; Ribeiro, F. H. *J. Catal.* **2003**, *217*, 233−239.
(58) Lin, J.-H.; Biswas, P.; Guliants, V. V.; Misture, S. *Appl. Catal., A* **2010**, *387*, 87−94.
(59) Chayakul, K.; Srithanratana, T.; Hengrasmee, S. *Catal. Today* **2011**, *175*, 420−429.
(60) Tabakova, T.; Boccuzzi, F.; Manzoli, M.; Andreeva, D. *Appl. Catal., A* **2003**, *252*, 385−397.
(61) Agnelli, M.; Swaan, H. M.; Marquez-Alvarez, C.; Martin, G. A.; Mirodatos, C. *J. Catal.* **1998**, *175*, 117−128.
(62) Badri, A.; Binet, C.; Lavalley, J.-C. *J. Chem. Soc., Faraday Trans.* **1996**, *92*, 4669−4673.
(63) Barrio, L.; Kubacka, A.; Zhou, G.; Estrella, M.; Martinez-Arias, A.; Hanson, J. C.; Fernandez-Garcia, M.; Rodriguez, J. A. *J. Phys. Chem. C* **2010**, *114*, 12689−12697.
(64) Betta, R. A. D. *J. Phys. Chem.* **1975**, *79*, 2519−2525.
(65) Yamasaki, H.; Kobori, Y.; Naito, S.; Onishi, T.; Tamaru, K. *J. Chem. Soc., Faraday Trans.* **1981**, *77*, 2913−2925.
(66) Bengaard, H. S.; Nørskov, J. K.; Sehested, J.; Clausen, B. S.; Nielsen, L. P.; Molenbroek, A. M.; Rostrup-Nielsen, J. R. *J. Catal.* **2002**, *209*, 365−384.
(67) Nakano, H.; Kawakami, S.; Fujitani, T.; Nakamura, J. *Surf. Sci.* **2000**, *454*−*456*, 295−299.
(68) Binet, C.; Daturi, M.; Lavalley, J.-C. *Catal. Today* **1999**, *50*, 207−225.
(69) Araki, M.; Ponec, V. *J. Catal.* **1976**, *44*, 439−448.
(70) Ichikawa, S.; Poppa, H.; Boudart, M. *J. Catal.* **1985**, *91*, 1−10.